# Inverse method for simultaneous determination of soil water flux density and thermal properties with a penta-needle heat pulse probe

Changbing Yang,[1,2] Masaru Sakai,[1,3] and Scott B. Jones[1]

[1] An accurate method for determination of in situ soil water flux density continues to be the most sought after and yet elusive hydrologic measurement. The penta-needle heat pulse probe (PHPP) employs a central heater needle surrounded by an orthogonal arrangement of four thermistor needles for two-component water flux density estimation. An analytical solution and inverse fitting method are presented for simultaneous estimation of thermal properties and soil water flux density using PHPP measurements. The approach yields estimates of both components of the flux in a plane normal to the axis of the PHPP needles. The method was evaluated using data measured by PHPPs in a laboratory experiment using a wide range of saturated water fluxes ranging from 1.2 to 33,200 cm d$^{-1}$. Improved water flux density determination was achieved from zero-flux adjusted estimates of the apparent heater-thermistor radii, $r_{adj}$, which were used in the inverse analysis. Thermal diffusivity and conductivity were estimated with coefficients of variation less than 1.35%, indicating that the inverse problem is well posed and yields unique parameter estimates when water flux is less than 2000 cm d$^{-1}$. Estimates of the $x$ and $y$ components of water flux density agreed well with measured water fluxes up to 7000 cm d$^{-1}$ exhibiting $R^2$ values greater than 0.976. Estimation of water flow direction based on 2-D water flux density was in good agreement with installation angle for water fluxes ranging from 10 to 7000 cm d$^{-1}$.

## 1. Introduction

[2] Soil water content and flux are the primary factors impacting subsurface processes which are of interest in scientific and engineering applications. Water content is the primary driver of plant and microbial activity in arid systems, and an array of measurement techniques have been developed for soil moisture assessment with continual improvements in sensor technology resulting in user-friendly and affordable measurement capabilities across the globe. However, determination of soil water flux density occurring near the surface or deeper in the subsurface remains a significant challenge despite the critical role for water flux in water balance estimates and for understanding the transport and fate of water, nutrients, and contaminants within the vadose zone.

[3] Over the last decade numerous studies on heat pulse measurements have shown promise for determination of soil thermal properties and water content [*Basinger et al.*, 2003; *Bristow*, 1998; *Bristow et al.*, 1993, 1994; *Campbell et al.*, 1991; *Ham and Benson*, 2004; *Heitman et al.*, 2003; *Knight et al.*, 2012; *Ochsner et al.*, 2003; *Ren et al.*, 2003; *Tarara and Ham*, 1997; *Welch et al.*, 1996; *Young et al.*, 2008]. Heat-pulse methods for measuring these physical properties are based on applying a heat pulse to a line source and then measuring the temperature increase about 6 mm from the source. The probes used for these measurements generally have two parallel needles, one containing the heat source and the other containing a thermistor or thermocouple.

[4] More recently, it has been shown that heat-pulse probes with an additional thermistor or thermocouple needle (three-needle probe) can be used to measure soil water flux density in addition to thermal properties and water content [*Gao et al.*, 2006; *Kamai et al.*, 2008; *Ochsner et al.*, 2005; *Ren et al.*, 2000]. The parallel, equidistant needles of these probes are configured to provide measurements of temperature rise directly upstream and directly downstream from the heater needle. Similar capabilities have been demonstrated with multifunctional heat-pulse probes, which allow for measurement of electrical conductivity in addition to soil water flux density, thermal properties, and water content [*Mori et al.*, 2003, 2005; *Mortensen et al.*, 2006]. To date, fluxes as small as $1.2 \times 10^{-7}$ m s$^{-1}$ (1 cm d$^{-1}$) [*Kamai et al.*, 2008, 2010] and as large as $3.1 \times 10^{-4}$ m s$^{-1}$ (2700 cm d$^{-1}$) [*Mori et al.*, 2005] have been resolved using three-needle and multifunctional heat-pulse probes. Considering this range of water flux density, such

---

[1]Department of Plants, Soils, and Climate, Utah State University, Logan, Utah, USA.

[2]Now at the Bureau of Economic Geology, University of Texas at Austin, Austin, Texas, USA.

[3]Now at the Graduate School of Bioresources, Mie University, Tsu, Japan.

Corresponding author: S. B. Jones, Department of Plants, Soils, and Climate, Utah State University, Logan, UT 84342, USA. (scott.jones@usu.edu)

sensors might be effectively used in soils with saturated hydraulic conductivities of similar magnitude for an assumed unit gradient under near-saturated conditions. This would include soils contained within three of six classes outlined in the National Soil Survey Handbook [*Soil Survey Staff*, 2003] and encompasses mean saturated hydraulic conductivity values from 9 of 11 soil classes listed in the UNsaturated SOils DAtabase (UNSODA) database [*Nemes et al.*, 2001].

[5] Although three-needle heat-pulse probes are useful for measuring soil water flux density, they are capable of quantifying only the component of the soil water flux density in a direction defined by the orientation of the needles. For fluxes of arbitrary magnitude and direction, additional thermistors are required to resolve the components of the flux. This is clear from the work of *Endo and Hara* [2003], in which a five-needle probe was used to quantify flux magnitude and direction in a plane normal to the needles of the probe. Like the arrangement employed in the multifunctional probes of *Mori et al*. [2003, 2005] and *Mortensen et al*. [2006], their five-needle probe consisted of a central heater needle surrounded by an orthogonal arrangement of four thermocouple needles. To quantify flux magnitude and direction, *Endo and Hara* [2003] developed an analytical inverse method to simultaneously estimate the soil thermal properties (i.e., diffusivity and heat capacity) and the two components of the flux in the presence of flow. Their novel inverse method is also presented in *Endo and Hara* [2007].

[6] Although the inverse method of *Endo and Hara* [2003, 2007] has considerable utility, it is important to recognize that the method is an approximate one. Specifically, the components of the flux are estimated using an approach similar to that proposed by *Wang et al*. [2002], which is known to yield only approximate estimates of soil water flux density [*Kluitenberg et al*., 2007]. Furthermore, in the inverse method of *Endo and Hara* [2003, 2007], estimates of the two flux components are used to estimate the thermal properties. Thus, any error in the estimates of the flux components will propagate to the estimated thermal properties. Clearly, it would be desirable to have an "exact" inverse method that eliminates the approximations.

[7] The objective of this study was to develop and evaluate an improved inverse method for use with heat-pulse probes having the five-needle configuration suggested by *Endo and Hara* [2003]. To obtain exact estimates of the relevant parameters, a new analytical solution was derived to account for the coupled conduction and convection of heat in two dimensions. The analytical solution is simultaneously fit to time series of temperature data from the four thermistor needles by using a Gauss-Newton-Levenberg-Marquardt method to minimize a generalized least-squares criterion. The inverse method was evaluated by performing a laboratory experiment with a penta-needle heat-pulse probe (PHPP) configuration similar to the sensor of *Endo and Hara* [2003]. Similar to the inverse method of *Endo and Hara* [2003, 2007], the inverse method presented herein allows for simultaneous estimation of soil thermal properties and the components of the soil water flux density from PHPP data collected in the presence of flow. Subsequently the computed magnitude and direction (angle) of water flux density may be calculated.
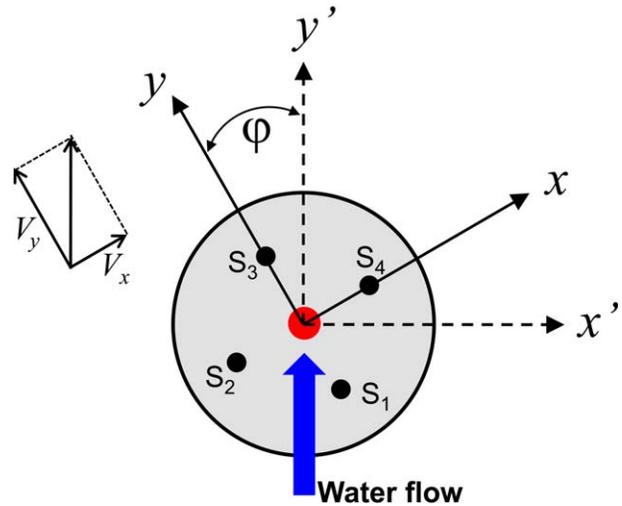


**Figure 1.** Schematic illustration of the PHPP showing the location of the heater needle and four thermistors ($S_1$, $S_2$, $S_3$, and $S_4$) in a plane normal to the axis of the probes (view from needle side of probe). To derive the analytical solution, the original coordinate system $(x, y)$ was rotated through angle $\varphi$ so that the $y'$ axis of the transformed coordinate system $(x', y')$ coincided with the direction of water flow. The components of the heat pulse velocity, $V_x$ and $V_y$, are used to determine the components of the soil water flux density.

## 2. Theory

### 2.1. Analytical Solution

[8] For uniform transport of water in an incompressible porous medium, the equation for combined heat conduction and convection in a 2-D domain (Figure 1), assuming that conductive heat transfer dominates over convective effects, is written as

$$\frac{\partial T}{\partial t} = \kappa\left(\frac{\partial^2 T}{\partial x^2} + \frac{\partial^2 T}{\partial y^2}\right) - V_x\frac{\partial T}{\partial x} - V_y\frac{\partial T}{\partial y} \quad (1)$$

where $T$ is the temperature ($^{\circ}$C), $\kappa$ is the bulk thermal diffusivity of the system (m$^2$ s$^{-1}$), $x$ and $y$ are spatial coordinates (m), $t$ is time (s), and $V_x$ and $V_y$ (m s$^{-1}$) are the components of the heat velocity vector, $\mathbf{V}$, in the $x$ and $y$ directions, respectively. The components of $\mathbf{V}$ can be expressed as

$$\begin{aligned} V_x &= \|\mathbf{V}\|\sin\varphi \\ V_y &= \|\mathbf{V}\|\cos\varphi \end{aligned} \quad (2)$$

where $\varphi$ is the angle of the flow direction with respect to the $y$ axis and $\|\mathbf{V}\|$ is the norm or magnitude of $\mathbf{V}$.

[9] We seek a solution of equation (1) for an infinite line source in an infinite, homogeneous medium with initial temperature $T(x, y, 0) = 0$. The line source, located at $(x, y) = (0, 0)$ and oriented normal to the $x$-$y$ plane, is heated at a constant rate during the time interval $0 < t \le t_0$. The desired analytical solution is obtained by making use of the transformation

$$\begin{pmatrix} x' \\ y' \end{pmatrix} = \begin{pmatrix} \cos\varphi & -\sin\varphi \\ \sin\varphi & \cos\varphi \end{pmatrix}\begin{pmatrix} x \\ y \end{pmatrix} \quad (3)$$

**Table 1.** Coordinates of the Four Thermistor Needles in the $x$-$y$ Plane[a]

| Thermistor | Location in $x$-$y$ Plane | |
| --- | --- | --- |
| | $x$ Coordinate | $y$ Coordinate |
| $S_1$ | 0 | $-r_1$ |
| $S_2$ | $-r_2$ | 0 |
| $S_3$ | 0 | $r_3$ |
| $S_4$ | $r_4$ | 0 |

[a]See Figure 1. The variables $r_1$–$r_4$ represent radial distances between the thermistor needles and the heater needle, where $r_i = \sqrt{x^2 + y^2}$.

where $x'$ and $y'$ are the new coordinates (Figure 1). This transformation, which rotates the coordinate system so that the $y'$ direction is aligned with the direction of water flow, allows equation (1) to be written in the form

$$\frac{\partial T}{\partial t} = \kappa \left( \frac{\partial^2 T}{\partial x'^2} + \frac{\partial^2 T}{\partial y'^2} \right) - \|\mathbf{V}\| \frac{\partial T}{\partial y'} \quad (4)$$

[10] For pulsed heating of an infinite line source, the solution of equation (4) is [*Ren et al.*, 2000]

$$T(x',y',t) = \begin{cases} \frac{q'}{4\pi\lambda} \int_0^t s^{-1} \exp\left[ -\frac{x'^2 + (y' - \|\mathbf{V}\|s)^2}{4\kappa s} \right] ds; & 0 < t \le t_0 \\ \frac{q'}{4\pi\lambda} \int_{t-t_0}^t s^{-1} \exp\left[ -\frac{x'^2 + (y' - \|\mathbf{V}\|s)^2}{4\kappa s} \right] ds; & t > t_0 \end{cases} \quad (5)$$

where $\lambda$ is thermal conductivity (W m$^{-1}$ °C$^{-1}$), $q'$ is the heat input per unit length per unit time (W m$^{-1}$), and $t_0$ is the heating duration (s).

[11] To write equation (5) in a form that satisfies equation (1), we make use of equation (3) to write it as

$$T(x,y,t) = \begin{cases} \frac{q'}{4\pi\lambda} \int_0^t s^{-1} \exp\left[ -\frac{(x\cos\varphi - y\sin\varphi)^2 + (x\sin\varphi + y\cos\varphi - \|\mathbf{V}\|s)^2}{4\kappa s} \right] ds; & 0 < t \le t_0 \\ \frac{q'}{4\pi\lambda} \int_{t-t_0}^t s^{-1} \exp\left[ -\frac{(x\cos\varphi - y\sin\varphi)^2 + (x\sin\varphi + y\cos\varphi - \|\mathbf{V}\|s)^2}{4\kappa s} \right] ds; & t > t_0 \end{cases} \quad (6)$$

[12] Upon making use of the identity $\|\mathbf{V}\|^2 = V_x^2 + V_y^2$ and the expressions in equation (2), equation (6) can be written in the form

$$T(x,y,t) = \begin{cases} \frac{q'}{4\pi\lambda} \int_0^t s^{-1} \exp\left[ -\frac{(x - V_x s)^2 + (y - V_y s)^2}{4\kappa s} \right] ds; & 0 < t \le t_0 \\ \frac{q'}{4\pi\lambda} \int_{t-t_0}^t s^{-1} \exp\left[ -\frac{(x - V_x s)^2 + (y - V_y s)^2}{4\kappa s} \right] ds; & t > t_0 \end{cases} \quad (7)$$

which is the desired solution of equation (1). Although this solution satisfies the initial condition $T(x,y,0) = 0$, equation (7) remains valid for a uniform, nonzero initial temperature, $T_0$, if we take $T(x,y,t)$ to represent the *temperature rise* above the initial value $T_0$. We make use of this generalization; however, for the sake of simplicity, we will refer to $T(x,y,t)$ as *temperature* instead of *temperature rise* hereafter. Expressions for temperature at the locations of the thermistors (i.e., thermistors $S_1$, $S_2$, $S_3$, and $S_4$ in Figure 1) can be obtained by substituting the coordinates for these locations (Table 1) into equation (7).

[13] Instead of $\kappa$ and $\lambda$, equation (7) could also be written in terms of $\kappa$ and $C$, which is the bulk volumetric heat capacity (J m$^{-3}$ °C$^{-1}$) of the system, a thermal property that is often more easily determined or known. This implementation in terms of the parameters $\kappa$, $C$, $V_x$, and $V_y$ uses the relation

$$C = \frac{\lambda}{\kappa} \quad (8)$$

[14] Furthermore, for purposes of needle spacing ($r$) calibration in the absence of water flow (i.e., $V_x = V_y = 0$),

spatial coordinates $x$ and $y$ in equation (7) may be substituted with $r$ ($r = \sqrt{x^2 + y^2}$), yielding

$$T(r,t) = \begin{cases} \frac{q'}{4\pi\kappa C} \int_0^t s^{-1} \exp\left[ -\frac{r^2}{4\,\kappa\,s} \right] ds; & 0 < t \le t_0 \\ \frac{q'}{4\pi\kappa C} \int_{t-t_0}^t s^{-1} \exp\left[ -\frac{r^2}{4\,\kappa\,s} \right] ds; & t > t_0 \end{cases} \quad (9)$$

[15] Both equations (7) and (9) model temperature rise due to a heat pulse allowing optimization of parameters related to combinations of thermal properties and heat velocities (5 degrees of freedom (DF) from parameters in equation (7)) or thermal properties and needle spacing (6 DF in equation (9) assuming $C$ is known), depending on the application. In the case of equation (7) we formulated the inverse method in terms of $\kappa$, $\lambda$, $V_x$, and $V_y$ because the partial derivatives used in the Jacobian matrix (section 2.2) have their simplest functional form when expressed in terms of $\kappa$ and $\lambda$. On the other hand, equation (9) is a special case of equation (7), providing a robust solution for calibration of needle spacing's under no flux conditions where estimates of $C$ are generally easier to compute or more available than $\lambda$.

## 2.2. Parameter Identification

[16] To estimate the parameters $\kappa$, $\lambda$, $V_x$, and $V_y$, we employed an inverse method that involved fitting temperature measurements from the PHPP to temperatures calculated using equation (7). The inverse method minimizes differences between measured and calculated temperatures for all four thermistors simultaneously.

[17] The most common tool for parameter identification is the generalized output least squares criterion [*Šimůnek*

*and Hopmans*, 2002]. Let **P** ($\kappa$, $\lambda$, $V_x$, and $V_y$) be the unknown parameter vector, then the objective function, $E$, can be expressed in terms of the least squares criterion as

$$E(\mathbf{P}) = \sum_{i=1}^{N}\sum_{j=1}^{4} w_i \left[ T_{i,j}^c(\mathbf{P}) - T_{i,j}^m \right]^2 = \sum_{i=1}^{N}\sum_{j=1}^{4} w_i R_{i,j}^2(\mathbf{P}) \qquad (10)$$

where $T_{i,j}^c(\mathbf{P})$ is the $i$th calculated temperature for the $j$th thermistor, $T_{i,j}^m$ is the $i$th measured temperature for the $j$th thermistor, $N$ is the total number of measured temperatures for each thermistor, $w_i$ is the weighting coefficient ($w_i = 1$ in this study) for the $i$th observation, and $R_{i,j}(\mathbf{P})$ is the $i$th residual for the $j$th thermistor.

[18] Several methods can be used to solve equation (10). In this study, the robust Gauss-Newton-Levenberg-Marquardt method was employed. Parameters at the $(k+1)$th iteration can be estimated from those at the $k$th iteration according to

$$\mathbf{P}^{k+1} = \mathbf{P}^k + \Delta\mathbf{P} = \mathbf{P}^k - \left(\mathbf{J}^T\mathbf{W}\mathbf{J}^T + \alpha\mathbf{I}\right)^{-1}\mathbf{J}^T\mathbf{W}\mathbf{R}(\mathbf{P}) \qquad (11)$$

where **I** is the identity matrix, $\alpha$ is the Marquardt parameter, **W** is the weight matrix (**W** = 1 in this study) in equation (10), **R** is the residual matrix in equation (10), and **J** is the Jacobian matrix, defined as

$$\mathbf{J} = \begin{bmatrix} \dfrac{\partial T_1^c}{\partial \kappa} & \dfrac{\partial T_1^c}{\partial \lambda} & \dfrac{\partial T_1^c}{\partial V_x} & \dfrac{\partial T_1^c}{\partial V_y} \\[2mm] \dfrac{\partial T_2^c}{\partial \kappa} & \dfrac{\partial T_2^c}{\partial \lambda} & \dfrac{\partial T_2^c}{\partial V_x} & \dfrac{\partial T_2^c}{\partial V_y} \\[2mm] \vdots & \vdots & \vdots & \vdots \\[2mm] \dfrac{\partial T_N^c}{\partial \kappa} & \dfrac{\partial T_N^c}{\partial \lambda} & \dfrac{\partial T_N^c}{\partial V_x} & \dfrac{\partial T_N^c}{\partial V_y} \end{bmatrix} \qquad (12)$$

[19] Closed-form expressions for the entries of **J** are given in Appendix A.

### 2.3. Estimation of Soil Water Flux Density

[20] Once the parameters $\kappa$, $\lambda$, $V_x$, and $V_y$ have been determined, the components of the soil water flux density vector, **J**, are estimated by making use of the relationships

$$\begin{aligned} J_x &= V_x \frac{C}{C_w} \\ J_y &= V_y \frac{C}{C_w} \end{aligned} \qquad (13)$$

where $J_x$ and $J_y$ are the components of the soil water flux density (m s$^{-1}$) in the $x$ and $y$ directions, respectively, and $C_w$ is the volumetric heat capacity of water. The estimates of $V_x$ and $V_y$ are used in equation (13) along with $C$, which is calculated from the estimates of $\kappa$ and $\lambda$ by using equation (8). The estimates of $J_x$ and $J_y$ can, in turn, be used to calculate both the magnitude and direction of the soil water flux density, whose magnitude is obtained from the expression

$$\|\mathbf{J}\| = \sqrt{J_x^2 + J_y^2} = \frac{C}{C_w}\sqrt{V_x^2 + V_y^2} \qquad (14)$$

and the direction of the water flux density in the $x$-$y$ plane is determined from

$$\varphi = \tan^{-1}\left(\frac{J_x}{J_y}\right) = \tan^{-1}\left(\frac{V_x}{V_y}\right) \qquad (15)$$

where a positive value of $\varphi$ indicates clockwise rotation from the $y$ axis reference as illustrated in Figure 1.

## 3. Materials and Methods

### 3.1. Penta-Needle Heat Pulse Probe (PHPP)

[21] The penta-needle heat pulse probe (PHPP) simultaneously determines soil thermal properties and the magnitude and direction of the soil water flux density within a plane normal to the needles. The probe consists of one 2.1 mm (OD) heater needle and four 1.27 mm (OD) parallel thermistor needles spaced 6.5 mm from the heater needle (center to center, Figure 1). Each opposing pair of thermistor needles provides one downstream and one upstream temperature measurement. The two pairs are orthogonally arranged at equal radial distance from the heater probe. The heater and thermistor needles were constructed using the procedures outlined by *Ham and Benson* [2004]. Each temperature-sensing needle contains a thermistor (10K3MCD1, BetaTherm Corp., Shrewsbury, MA) epoxied at the distal end of the tubing. The heater needle was made from two loops (four strands total) of enameled Nichrome resistance wire (Nichrome 80, Pelican Wire Co., Naples, FL) also secured using thermally conductive epoxy. The heater and thermistor needles were soldered to a circuit board and potted into a 23.6 mm (ID) polyvinyl chloride tube using epoxy. The heater needle extended 28 mm from the epoxy body while the thermistor needles protruded 16 mm. The precision and stability of temperature measurement is a critical factor for water flux density estimation, especially at low fluxes where differences between upstream and downstream temperatures are small. The precision of thermistors used in the PHPP were evaluated by measuring temperature every 5 s for 10 min in an insulated container filled with wet sand. The resulting temperature fluctuations were less than 0.001°C.

[22] The PHPP was connected to and communicated with a datalogger (Model CR1000, Campbell Scientific Logan, UT) via SDI-12 communication. The PHPP includes an onboard microcontroller with a 12 bit analog to digital converter for control of the heat pulse (8 s) and measuring temperature at each thermistor needle for a period of as much as 120 s. To determine the heating rate, average current through the heater wire was determined by sampling the voltage drop across a precision 1 $\Omega$ resistor in series with the heater probe. Initial temperature was measured immediately before applying the heat input. The microcontroller can perform onboard optimization of parameters $\kappa$, $\lambda$, $V_x$, and $V_y$ using the temperature rise data with additional calculations performed on the datalogger, i.e., heat capacity, water flux density, and direction. However, for this study, measured temperature rise values were downloaded to the datalogger for postprocessing and parameter optimization using a computer.

### 3.2. Implementation of the Inverse Parameter Optimization Method

[23] The inverse method for optimizing thermal properties and water flux density in soils from temperature

measurements of the PHPP was implemented in a Fortran program named INV-WATFLX [*Yang and Jones*, 2009], which shares some inverse subroutines from Inverse-CORE [*Dai and Samper*, 2004; *Yang et al.*, 2008]. The INV-WATFLX code simultaneously fits temperature measurements from the four thermistors surrounding the heater, but it also provides the option (not employed in this study) of fitting temperature differences from the orthogonal pairs of thermistors.

[24] Since the Newton-Gauss-Levenberg-Marquard method is used in INV-WATFLX, initial estimates of $\kappa$, $\lambda$, $V_x$, and $V_y$ must be specified. These estimates were obtained by implementing a variety of "single point" estimation methods in INV-WATFLX. To estimate $\kappa$, we used the expression [*Bristow et al.*, 1994],

$$\kappa = \frac{r^2}{4} \left[ \frac{\frac{1}{t_m - t_0} - \frac{1}{t_m}}{\ln\left(\frac{t_m}{t_m - t_0}\right)} \right] \qquad (16)$$

where $r$ is the mean heater- to thermistor-needle spacing of the four thermistors illustrated in Figure 1, $t_m$ is the time from the initiation of heating to the occurrence of the maximum temperature, $T_{max}$. To estimate $\lambda$, we made use of an expression for $C$ from *Knight and Kluitenberg* [2004] to write

$$\lambda = \kappa C = \frac{\kappa q' t_0}{e \pi r^2 T_{max}} \left( 1 - \frac{\varepsilon^2}{8} \left\{ \frac{1}{3} + \varepsilon \left[ \frac{1}{3} + \frac{\varepsilon}{8} \left( \frac{5}{2} + \frac{7\varepsilon}{3} \right) \right] \right\} \right) \qquad (17)$$

where $e$ is the logarithmic constant ($\sim$2.718) and $\varepsilon = t_0 / t_m$. The INV-WATFLX code analytically evaluates $\kappa$ and $\lambda$ at each of the four thermistors using equations (15) and (16), with average values being used as initial estimates. Initial estimates of $V_x$ and $V_y$ were obtained using the expressions [*Wang et al.*, 2002]

$$\begin{aligned} V_x &= \frac{2\kappa}{r_2 + r_4} \ln \frac{T_4}{T_2} \\ V_y &= \frac{2\kappa}{r_1 + r_3} \ln \frac{T_3}{T_1} \end{aligned} \qquad (18)$$

where $r_i$ is the heater- to thermistor-needle spacing as defined in Table 1 and $T_i$ is the temperature at $t = 60$ s of the $i$th thermistor needle. Although the expressions in equation (18) are strictly valid only as $t \rightarrow \infty$, the results of *Gao et al.* [2006], *Mori et al.* [2003], and *Ochsner et al.* [2005] indicate that the approximation of *Wang et al.* [2002] is best implemented using temperature data for times ranging from 40 to 90 s. We selected a 60 s analysis in our testing.

[25] Convergence of the inverse method in INV-WATFLX is determined by assessing relative changes in parameter values and relative changes in the value of the objective function. A tolerance of $10^{-30}$ was used for the parameters $\kappa$, $\lambda$, $V_x$, and $V_y$, and a tolerance of $10^{-7}$ was used for the objective function, $E(\mathbf{P})$. When one of the two convergence conditions is satisfied, INV-WATFLX stops and outputs the optimized parameter values.

[26] As described in section 2.3, the estimates of $\kappa$, $\lambda$, $V_x$, and $V_y$ obtained using INV-WATFLX can be used to calculate the bulk volumetric heat capacity, $C$, and the two components of the soil water flux density. These components, $J_x$ and $J_y$, can then be used to obtain the magnitude and direction of the water flux. In addition, $C$ can also be used to estimate the soil volumetric water content, $\theta$, by making use of the expression

$$\theta = \frac{C - \rho_b c_s}{C_w} \qquad (19)$$

where $\rho_b$ is soil bulk density (Mg m$^{-3}$) and $c_s$ is the specific heat capacity of the soil solids (J kg$^{-1}$ °C$^{-1}$).

## 3.3. Heater-Thermistor-Needle Spacing Calibration

[27] One of the challenges for obtaining accurate measurements using radiating heat pulse techniques is in accurately determining the distance between the heater- and temperature-sensing-needle, whose position coordinate or spacing is squared in equations (7) and (9). It is therefore imperative that the apparent spacing, $r$ (not necessarily the physical distance), be determined accurately [*Mori et al.*, 2003, 2005], especially for low water flux densities (e.g., $<$100 cm d$^{-1}$). Historically $r$ was determined in the laboratory using water stabilized with 6 g L$^{-1}$ agar [e.g., *Ham and Benson*, 2004], a scenario in which the volumetric heat capacity of water is known ($C_w = 4.18 \times 10^6$ J m$^{-3}$ °C$^{-1}$). However, this calibration approach falls short of accounting for in situ factors affecting determination of $r$ such as contact resistance, substrate heterogeneity [*Knight et al.*, 2012], and potential needle deflection from insertion. For saturated flow conditions tested here, we used the following calibration approach which includes use of the parameter optimization method described previously.

[28] The in situ PHPP needle spacing calibration was carried out by taking 120 temperature measurements, initiated with the 8 s heat pulse in the saturated sand column under static conditions (i.e., $V_x = V_y = 0$). Equation (9) was then fit to these data by optimizing $\kappa$ in addition to $r_1$ through $r_4$. It is assumed that an independent measurement or estimate of the bulk volumetric heat capacity, $C$, is possible, an approach previously implemented in laboratory investigations [*Mori et al.*, 2003; *Mortensen et al.*, 2006]. The bulk volumetric heat capacity can be estimated using equation (7) fit to temperature rise data using default needle spacing values or in this study computed from known properties using the following expression;

$$C = \rho_b c_s + C_w \theta \qquad (20)$$

where $\rho_b$ of sand was 1460 kg m$^{-3}$ (45% porosity) and specific heat capacity of quartz was taken as 830 J kg$^{-1}$ °C$^{-1}$ [*Jury and Horton*, 2004]. We assumed complete saturation due to packing sand in a water-filled column as described in section 3.4. This resulted in a bulk heat capacity of 3.09 $\times 10^6$ J m$^{-3}$ °C$^{-1}$. The procedure for in situ needle spacing calibration is summarized in Table 2.

## 3.4. Laboratory Experiment

[29] A set of 1-D flow column experiments (Figure 2) were carried out to test the PHPP in a saturated coarse silica sand (2075, Industrial Quartz, Unimin Corp., Emmett, ID) to facilitate testing at high water flux

**Table 2.** Outline of Equations and Parameters Used for Determination of $r$ With In Situ Spacing Calibration and Zero-Flux Adjusted Spacing Calibration Procedures

| | In Situ Calibration | Zero-Flux Adjusted Calibration |
|---|---|---|
| Symbol | $r_{ins}$ | $r_{adj}$ |
| Fitting equation | Equation (9) | Equation (7) |
| Fixed parameters | $C$, $V_x = V_y = 0$ | |
| Optimized parameters | $\kappa$, $r_1$, $r_2$, $r_3$, $r_4$ | $\kappa$, $\lambda$, $V_x$, $V_y$ |
| Iterative procedure | | Optimize $r_1 \sim r_4$ so that $\Delta r_x$ and $\Delta r_y < 10^{-5}$ (equation (21)) |

densities. Three PHPPs were installed perpendicular to flow in a 40 cm tall by 5 cm inner diameter column at uniform intervals of 10 cm between probes. The column was packed with sand in the water-filled column to eliminate air entrapment. To test the estimation of flow angle, the PHPPs installed at the top, center, and bottom of the column were oriented to yield water flow directions, $\varphi$, of 15° (labeled PHPP$_{15°}$ hereafter), 30° (PHPP$_{30°}$), and 45° (PHPP$_{45°}$), respectively (Figure 1). Water flow in the sand column was from bottom to top and varied across 25 different water flux densities ranging from 1.2 to 33,200 cm d$^{-1}$ (1.4 × 10$^{-7}$ to 3.8 × 10$^{-3}$ m s$^{-1}$) including a no-flow, static condition. Water was delivered to the column at fixed rates using a precision syringe pump (KDS 230, KD Scientific, Holliston, MA) for flow rates less than 1000 cm d$^{-1}$. For flow rates greater than 1000 cm d$^{-1}$, a peristaltic pump (Masterflex, Cole-Parmer, Vernon Hills, IL) was used

(Figure 2). For each flow rate setting, the steady state rate was verified by measuring water discharge from the column in 5 s intervals using an analytical balance interfaced with the datalogger. Actual water flow rates were determined from the balance output.

[30] Each PHPP measurement cycle began with an initial temperature measurement followed by an 8 s heat pulse (approximately 165 W m$^{-1}$). With the initiation of the heat pulse, temperature-time data, $T(t)$, from the four thermistors were recorded simultaneously at 1 s intervals (i.e., every second for each thermistor) for a duration of 120 s. The average current applied to the heating needle was also recorded to accurately determine heat pulse intensity, $q'$. To avoid thermal interference between probes, each measurement cycle began with the probe furthest downstream (top) and measurements proceeded upstream at 2 min intervals. Three repetitions of each PHPP measurement were carried out at 20 min intervals for each flow rate before moving to the next flow rate setting. The recorded $T(t)$ data at the four thermistors were used to simultaneously estimate parameters $\kappa$, $\lambda$, $V_x$, and $V_y$ by fitting equation (7) using INV-WATFLX. Initial estimates of the four parameters were calculated according to equations (16)–(18) as previously discussed.

[31] To verify the PHPP estimation of thermal properties, the thermal conductivity of the same saturated sand was independently measured using a single-needle KD2-Pro (Decagon Device) [e.g., *Smits et al.*, 2010]. The thermal diffusivity was independently estimated (equation (8)) from the KD2-Pro measured thermal conductivity and the volumetric heat capacity calculated from the bulk density (section 3.3).
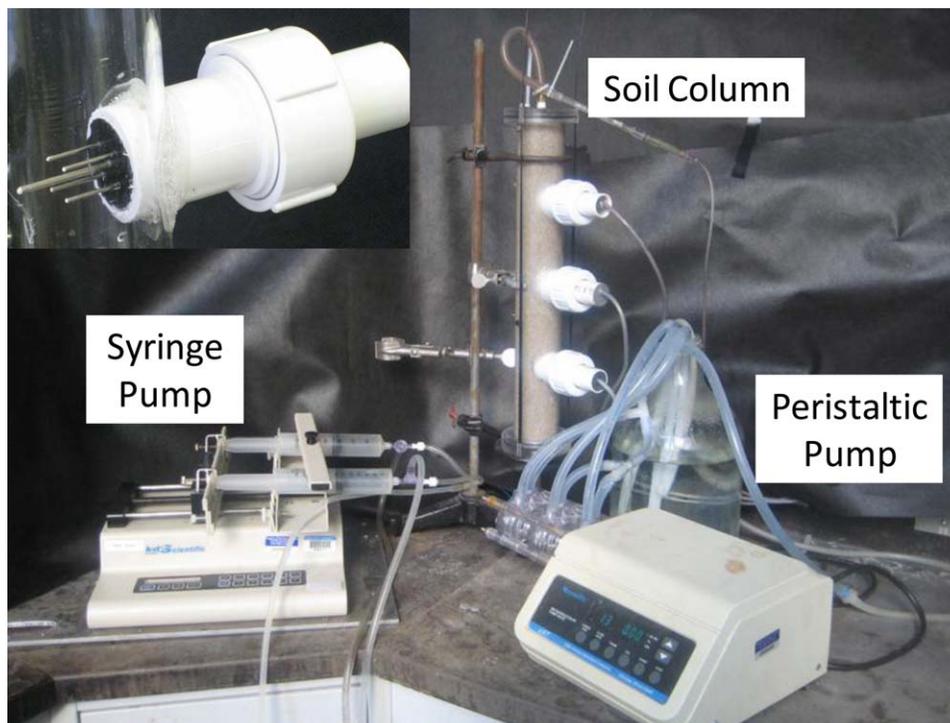


**Figure 2.** Experimental 1-D flow column filled with sand and fed with water (upward flow) from a precision syringe pump or a peristaltic pump. Three PHPPs (Figure 1) were installed with the needles oriented to give water flow directions of $\varphi =$ (top) 15°, (center) 30°, and (bottom) 45°.

**Table 3.** Apparent Needle Spacings, $r$, of Each PHPP Used in the Parameter Optimization[a]

| | Thermistor | Agar | | In Situ | | Adjusted |
|---|---|---|---|---|---|---|
| | | $r_{agar}$ (mm) | $\kappa$ ($10^{-7}$ m$^2$ s$^{-1}$) | $r_{ins}$ (mm) | $\kappa$ ($10^{-7}$ m$^2$ s$^{-1}$) | $r_{adj}$ (mm) |
| | S$_1$ | 6.134 (0.00180) | 1.464 (0.0010) | 6.249 (0.01170) | 6.827 (0.0531) | 6.321 |
| | S$_2$ | 6.253 (0.00188) | | 6.260 (0.00663) | | 6.234 |
| PHPP$_{15°}$ | S$_3$ | 6.193 (0.00196) | | 6.176 (0.00414) | | 6.113 |
| Top | S$_4$ | 6.272 (0.00299) | | 6.261 (0.00606) | | 6.288 |
| | S$_1$ | 6.274 (0.00321) | 1.566 (0.0012) | 6.272 (0.00799) | 7.217 (0.0514) | 6.385 |
| | S$_2$ | 6.549 (0.00224) | | 6.319 (0.00795) | | 6.312 |
| PHPP$_{30°}$ | S$_3$ | 6.324 (0.00155) | | 6.068 (0.00320) | | 5.955 |
| Center | S$_4$ | 6.075 (0.00198) | | 5.928 (0.00348) | | 5.935 |
| | S$_1$ | 6.372 (0.00849) | 1.518 (0.0012) | 6.601 (0.00625) | 7.050 (0.0580) | 6.646 |
| | S$_2$ | 6.426 (0.00130) | | 6.499 (0.00868) | | 6.471 |
| PHPP$_{45°}$ | S$_3$ | 6.114 (0.00223) | | 5.886 (0.00358) | | 5.842 |
| Bottom | S$_4$ | 6.111 (0.00201) | | 5.901 (0.00475) | | 5.929 |

[a]Determinations made in agar-stabilized water ($r_{agar}$), in situ in a sand column ($r_{ins}$), and adjusted to match measured known water flux density (i.e., 0 cm d$^{-1}$ under static conditions) in the sand column ($r_{adj}$). Values of $r$ and $\kappa$ are given with standard deviations in brackets for $r_{agar}$ and $r_{ins}$. Because $r_{adj}$ is determined using a different approach only the adjusted value is shown here.

## 4. Results and Discussion

[32] Given the previously described theoretical and experimental conditions, we set out to test the PHPP thermal property and water flux density determination capabilities. We first demonstrate improvements in parameter estimation realized using in situ spacing calibration compared to calibration in agar. We then demonstrate the consistency of thermal properties determined as a function of varied water flow rates. The PHPP heat flux estimates, $V_x$ and $V_y$, are then used to compute water flux density values for comparisons with known flow rates using the different spacing calibration results. It was at this stage of our research that we developed a novel technique for improving water flux density measurement resolution near 1 cm d$^{-1}$ using a flux-adjusted spacing calibration. Our presentation is concluded by comparing the directional water flux density determination capability of the PHPP.

### 4.1. Fitting the Analytical Solution to Temperature Rise Data

[33] Table 3 shows apparent spacing, $r$, between the heater needle and each thermistor needle, S$_1$–S$_4$ (Figure 1). The calibrated apparent spacing in agar ($r_{agar}$) for all four thermistors was smaller than the center-to-center physical needle spacing of 6.5 mm. As *Mori et al.* [2003] mentioned, variations in the position of the epoxy-embedded thermistor within the steel tubing can contribute to these differences. *Knight et al.* [2012] simulated faster heat pulse arrival time due to the finite needle radius, which also leads to smaller apparent spacing. Values of $r$ were also determined in the saturated sand column ($r_{ins}$) under a no-flow condition, in situ, where values of $r_{ins}$ in Table 3 are substantially different from the $r_{agar}$ values with the maximum difference of 0.256 mm for thermistor 3 (S$_3$) in PHPP$_{30°}$. These differences may be attributed to any number of factors including different contact resistance between the sand and needle or modified thermal properties resulting from heterogeneities of the sand-water system [*Mori et al.*, 2003]. Using the predetermined apparent spacings ($r_{agar}$ and $r_{ins}$), the parameters $\kappa$, $\lambda$, $V_x$, and $V_y$ were optimized with a computer by fitting the analytical solution (equation (7)) to temperature rise data using the INV-WATFLX code. Figure 3 shows two examples of measured temperature rise data with a 15° orientation angle (PHPP$_{15°}$) at water flux densities of 98 cm d$^{-1}$ (Figure 3a) and 3830 cm d$^{-1}$ (Figure 3b) with the fitted analytical solutions obtained from $r_{ins}$. As shown in Figure 1, thermistors S$_1$ and S$_3$ on the $y$ axis were rotated counterclockwise from the vertical direction, while $x$ axis thermistors S$_2$ and S$_4$, were rotated from the horizontal plane. For this scenario of vertical upward water flow, thermistors S$_1$ and S$_2$ lie upstream while S$_3$ and S$_4$ are downstream. For the relatively small water flux density of 98 cm d$^{-1}$ (Figure 3a), the furthest measured downstream temperature (S$_3$) exhibited the maximum temperature rise with the peak value of 1.4°C, while the minimum temperature rise upstream (S$_1$) shows a peak value of 1.16°C. Since the $x$ axis is more orthogonal to the water flow direction, the temperature rise difference between upstream and downstream for the $x$ axis thermistors (S$_2$ and S$_4$) was smaller than the $y$ axis values. At the higher water flux density of 3830 cm d$^{-1}$ (Figure 3b), thermistor S$_3$ exhibited an extremely large temperature spike of up to 4.8°C, while the other three values were less than 0.6°C. This illustration highlights the capacity of this method to resolve a wide range of water flux densities based on spatially dependent temperature differences with differential measurement resolution on the order of 0.001°C. Analytical solutions fitted to measured temperature rise curves are also shown in Figure 3. The analytical solution using $r_{ins}$ shows good agreement with measured data for both examples, indicating the solution is applicable for a wide range of water flux densities.

### 4.2. Thermal Properties

[34] Figure 4 shows the relation between estimated thermal properties by the PHPP with an installation angle of 30° (PHPP$_{30°}$) as a function of the measured sand column water flux density. Thermal diffusivity, $\kappa$ (Figure 4a), and thermal conductivity, $\lambda$ (Figure 4b), were optimized by fitting the analytical solution (equation (7)) to the four measured temperature rise data sets, while bulk volumetric heat capacity, $C$ (Figure 4c), was calculated from optimized $\kappa$ and $\lambda$ using equation (8). Independently measured or
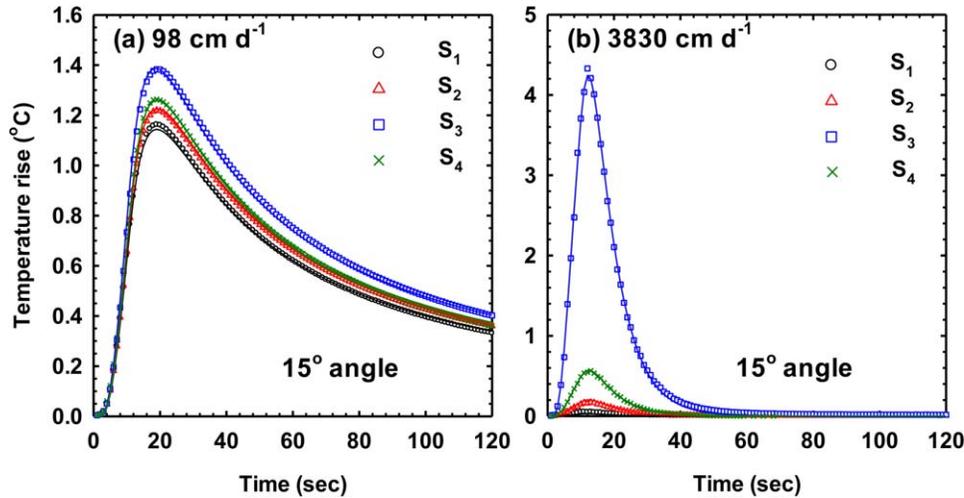
**Figure 3.** Illustration of inverse fitting of the analytical solution (equation (7)) to measured temperature rise from each of the four PHPP thermistors installed at a 15° angle. Measurements reflect water flux densities of (a) 98 cm d$^{-1}$ and (b) 3830 cm d$^{-1}$. The solid lines are the analytically modeled temperature trace using the $r_{ins}$ determined spacing.

estimated thermal diffusivity (7.02 m$^2$ s$^{-1}$), thermal conductivity (2.17 W m$^{-1}$ °C$^{-1}$), and volumetric heat capacity (3.09 × 10$^6$ J m$^{-3}$ °C$^{-1}$) were also plotted in Figure 4. All three thermal properties exhibited consistent values for water flux densities less than 2000 cm d$^{-1}$ (maximum value of 1530 cm d$^{-1}$). Optimized $\kappa$ values using $r_{agar}$ (7.59 ± 0.066 × 10$^{-7}$ m$^2$ s$^{-1}$, $c_v = 0.86\%$) were slightly larger than the optimized $\kappa$ using $r_{ins}$ (7.21 ± 0.067 × 10$^{-7}$ m$^2$ s$^{-1}$, $c_v = 0.93\%$), and the optimized $\kappa$ values using $r_{ins}$ were closer to the individually estimated $\kappa$ value of saturated sand. The needle spacing effect on $\lambda$ optimization was small, and the mean and standard deviations using $r_{agar}$ and $r_{ins}$ were 2.24 ± 0.016 W m$^{-1}$ °C$^{-1}$ (coefficient of variation, $c_v = 0.71\%$) and 2.25 ± 0.014 W m$^{-1}$ °C$^{-1}$ ($c_v = 0.61\%$), respectively, for the range of infused water flux densities less than 2000 cm d$^{-1}$ (Table 3). Both of these optimized $\lambda$ values were in reasonable agreement with an independently measured (KD2-pro) value of 2.17 W m$^{-1}$ °C$^{-1}$. The other parameter, $C$, calculated as 3.09 × 10$^6$ J m$^{-3}$ °C$^{-1}$ from optimized $\kappa$ and $\lambda$ was in better agreement using $r_{ins}$ (2.95 ± 0.016 × 10$^6$ J m$^{-3}$ °C$^{-1}$, $c_v = 0.53\%$ for $r_{agar}$ and 3.12 ± 0.021 × 10$^6$ J m$^{-3}$ °C$^{-1}$, $c_v = 0.67\%$ for $r_{ins}$). The volumetric water content, $\theta$, calculated from equation (19) with the computed $C$ value showed excellent agreement using $r_{ins}$ with $\theta = 0.456 ± 0.005$ cm$^3$ cm$^{-3}$ for 45% porosity, while $r_{agar}$ underestimated $\theta$ at 0.417 ± 0.004 cm$^3$ cm$^{-3}$. Mean, standard deviation, and coefficient of variation were computed for each thermal property from all PHPP measured water flux densities below 2000 cm d$^{-1}$, shown in Table 3. All three PHPPs produced reasonably similar estimates with small standard deviation and coefficient of variation, $c_v$. Considering probe-to-probe variation, we estimated $C$ using $r_{ins}$ combining results from all three PHPPs yielding a mean value of 3.13 × 10$^6$ J m$^{-3}$ °C$^{-1}$ and standard deviation of 0.005 × 10$^6$ J m$^{-3}$ °C$^{-1}$ with $c_v$ equal to 0.15%. In addition, the three-probe average values of $\kappa$ and $\lambda$ were also relatively similar among individual probe means and standard deviations. Calibration spacings using $r_{agar}$

produced $\kappa$ standard deviations and $c_v$ values twice as large as the other two methods, but calibration choice had little impact on $\lambda$ statistics.

[35] For water flux densities exceeding 2000 cm d$^{-1}$, a velocity-dependent increase in $\kappa$, $\lambda$, and consequently in $C$ is seen in Figures 4a–4c. *Hopmans et al.* [2002] hypothesized that it may be necessary to account for the effect of hydrodynamic dispersion on soil thermal properties for high water velocity, which *Sisodia and Helweg* [1998] included in their thermal conductivity model. The lack of velocity dependence in our models used to estimate $\kappa$ and $\lambda$ (Figure 4) corroborates the apparent significance of thermal dispersion for fluxes greater than 2000 cm d$^{-1}$ for the sand evaluated. The velocity dependence is also consistent with the results of *Mori et al.* [2005], *Mortensen et al.* [2006], *Ochsner et al.* [2005], and *Gao et al.* [2006]. It is important to note that the velocity dependence of $\kappa$ and $\lambda$ is clearly exhibited here only because this particular inverse method allowed for thermal property estimation. Since the heat capacity of the sand-water mixture is a constant, the computed increase in $C$ is a further indicator of errors in accurate thermal property optimization at higher water flux densities (Figure 4c).

### 4.3. Soil Water Flux Density

[36] Water flux density can be estimated from optimized heat velocities ($V_x$ and $V_y$) and thermal properties using equation (13). Figures 5a and 5b show the comparison between $x$ ($J_x$) and $y$ ($J_y$) component water flux densities estimated by PHPP$_{15°}$ (i.e., installed at a 15° angle relative to flow direction). Note that the horizontal axes in Figures 5a and 5b are the computed $x$ and $y$ components derived by multiplying the measured column outlet flux magnitude by the vector information (i.e., sin $\varphi$ for $x$ component and cos $\varphi$ for $y$ component, see Figure 1). Both estimates of $J_x$ using $r_{agar}$ and $r_{ins}$ agreed well with the $x$ component of measured flux between 25 and 1550 cm d$^{-1}$, corresponding to water flux density magnitudes of between 98 and 6000 cm d$^{-1}$. Estimates of $J_y$ using $r_{agar}$ and $r_{ins}$ also agreed well
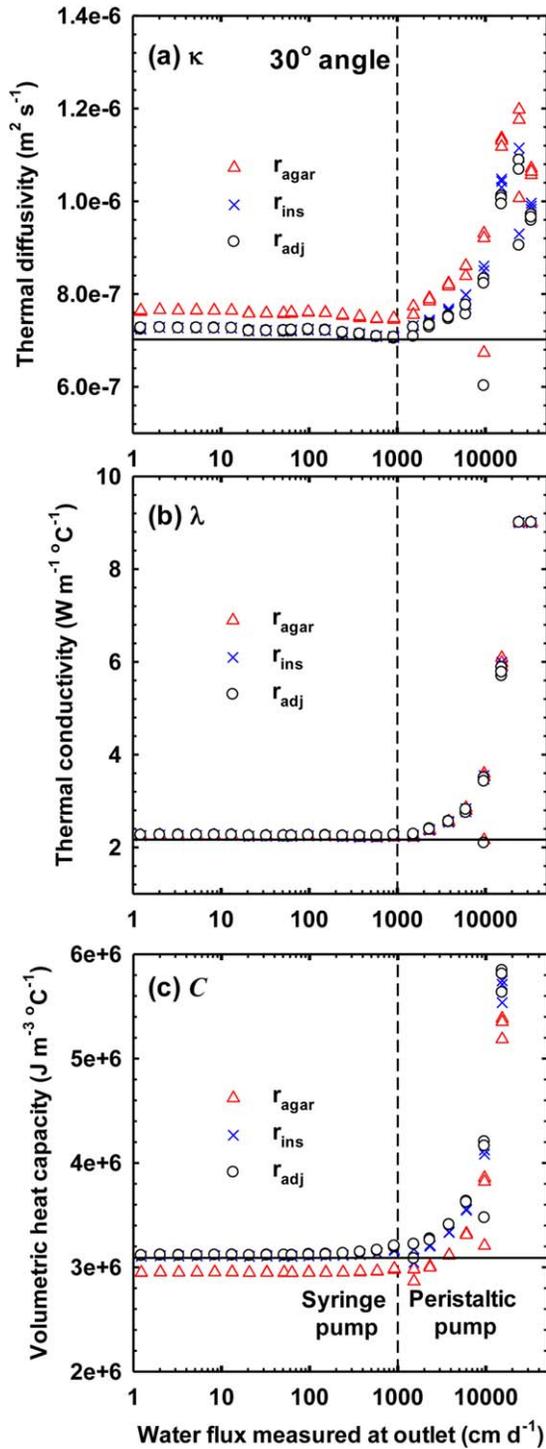
**Figure 4.** Thermal properties optimized from PHPP measurements showing (a) thermal diffusivity, $\kappa$, (b) thermal conductivity, $\lambda$, and (c) estimated bulk volumetric heat capacity, $C$, versus water flux density measurements at the outlet. Triangle, cross, and circle symbols indicate estimates using calibrated spacings in agar ($r_{agar}$), in situ saturated sand ($r_{ins}$), and using an zero-flux adjusted spacing ($r_{adj}$), respectively. Solid lines are independently measured or estimated values under static conditions. Water flux densities less than 1000 cm d$^{-1}$ were controlled by a syringe pump, while those above were controlled by a peristaltic pump.
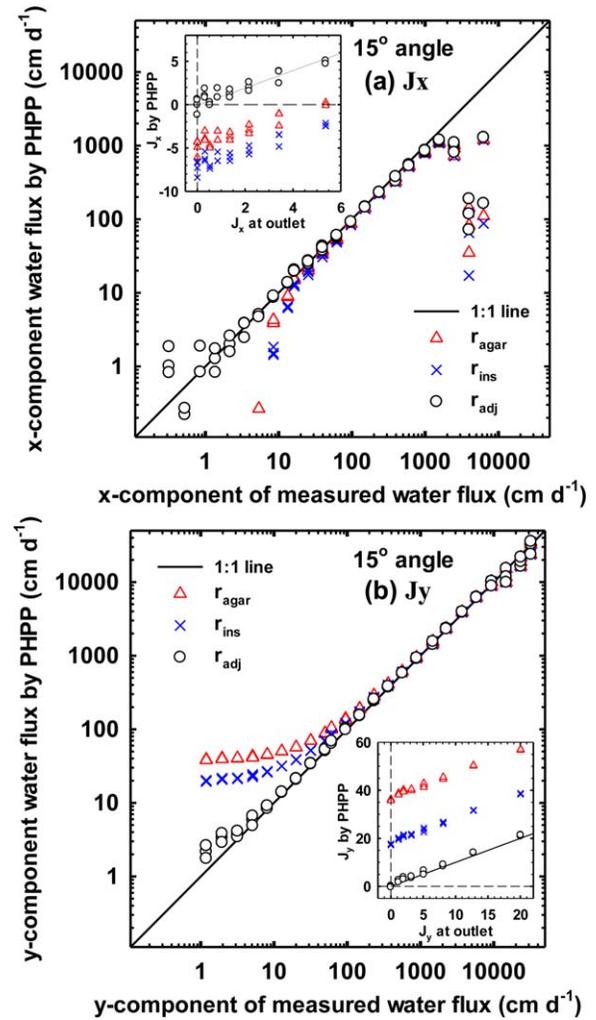
**Figure 5.** Estimated (a) $x$ and (b) $y$ components of water flux density by the PHPP installed with the 15° rotation angle. Horizontal axes indicate the $x$ or $y$ component of measured water flux density as adjusted by the probe installation angle. Inset figures show reduced water flux density ranges (i.e., $\leq$20 cm d$^{-1}$) including the no flux (0 cm d$^{-1}$) estimates. Note the linear scale used for inset figures. Triangle, cross, and circle symbols represent results using calibrated spacings in agar ($r_{agar}$), in situ saturated sand ($r_{ins}$), and using zero-flux adjusted spacing ($r_{adj}$), respectively.

with measured fluxes above 95 cm d$^{-1}$ corresponding to magnitudes greater than 98 cm d$^{-1}$. For flux rates above 2000 cm d$^{-1}$, estimates of $J_x$ were irreconcilable because vertical heat transport overwhelms horizontal with increasing water flux density, where S$_2$ and S$_4$ are horizontally displaced further from the heater than S$_1$ and S$_3$. Estimates of $J_y$ were reasonable beyond our upper flow rate (i.e., 33,200 cm d$^{-1}$), suggesting even higher water flux density measurement capability for flow estimates where three needles are oriented with the flow direction. For low flux rates, estimates of $J_x$ and $J_y$ were underestimated and overestimated, respectively. Note that some $J_x$ data do not appear in the log-log scaled graph in Figure 5a because of negative results. Inset figures use a linear scale to provide details of the low flux range below 20 cm d$^{-1}$, where estimates of $J_x$
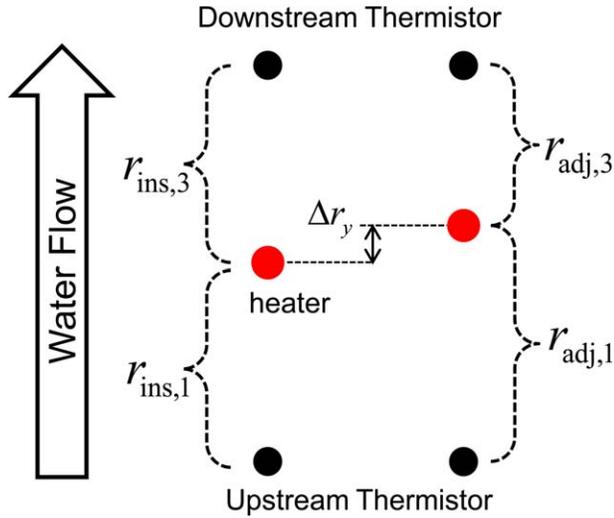
**Figure 6.** Schematic diagram of zero-flux adjusted spacing ($r_{adj}$) calibration which uses $r_{ins}$ spacing values along with perturbations ($\Delta r_x$ and $\Delta r_y$) in the apparent heater location to determine $r_{adj}$ values for all four thermistor needles shown in Figure 1.

and $J_y$ increased linearly with increasing water flux density. However, when using $r_{agar}$, $J_x$ was underestimated by about 5 cm d$^{-1}$ and $J_y$ was overestimated by about 37 cm d$^{-1}$ relative to the 1:1 line. Use of $r_{ins}$ in place of $r_{agar}$ yielded a worse estimate in $J_x$ and improvement in the flux prediction of $J_y$ as illustrated in Figure 5 (i.e., −6 cm d$^{-1}$ for $J_x$ and 19 cm d$^{-1}$ in $J_y$). As mentioned in section 3.3, $r_{ins}$ was determined by fitting the analytical solution (equation (9)) to measured temperature rise data under a no-flow condition, assuming $V_x$ and $V_y$ were zero. In spite of the no-flow assumption, estimates of $J_x$ and $J_y$ optimized by fitting equation (7) with predetermined $r_{ins}$ are nonzero, i.e., estimates should be 0 cm d$^{-1}$ on the horizontal axes in Figure 5. This "nonzero" discrepancy may result from a combination of measurement error coupled with poor fitting of the observed temperature rise data using the analytical solution (e.g., $S_3$ in Figure 3b). In order to reduce these discrepancies, we address yet a third calibration approach that was

discovered in the midst of attempting to better estimate these low water flux densities. It came about as we sought to address the asymptotic water flux density estimates between 10 and 100 cm d$^{-1}$ shown in Figures 5a and 5b.

#### 4.3.1. Calibration of Zero-Flux Adjusted Spacing

[37] The increasing sensitivity of water flux density determination on $r$ values below 100 cm d$^{-1}$ arises from the reducing temperature differences upstream and downstream coupled with the squaring of $r$ in equation (7). Assuming $r_{ins}$ could be improved using the known, i.e., zero-flux rate, we carried out additional fine tuning of $r$ calibration in order to improve estimates of low water flux density to extend the range for this measurement method.

[38] Theoretically, if the upstream spacing and the downstream spacing are equal, the temperature rise downstream will always be higher than the upstream values for any flow condition. In reality, if the thermistor spacing downstream were greater than upstream, an opposite result could occur, especially at low water flux densities. For example, estimated $J_y$ values in Figure 5b were up to an order of magnitude larger than the actual flux densities; therefore, the impact of heater-thermistor-needle spacings, $r_{ins,i}$, on the $y$ coordinate flux estimate was reevaluated. To reduce the overestimation of $J_y$, either the apparent spacing, $r_{ins,1}$, for thermistor needle 1 ($S_1$ in Figure 1), located upstream should be larger or the $r_{ins,3}$ value for $S_3$ located downstream should be smaller. We found that changing both $r$ values by the same amount (equal but opposite sign) simplified the algorithm, thereby maintaining a constant absolute distance between $S_1$ and $S_3$ obtained from $r_{ins}$ (see Figure 6). In the same way, the underestimation of $J_x$, was reanalyzed using a smaller $r$ value for $S_2$ located upstream and a larger $r$ value was used for $S_4$. Based on this concept, four new $r$ values were obtained as follows:

$$r_{adj,1} = r_{ins,1} + \Delta r_y; \quad r_{adj,3} = r_{ins,3} - \Delta r_y$$
$$r_{adj,2} = r_{ins,2} + \Delta r_x; \quad r_{adj,4} = r_{ins,4} - \Delta r_x \qquad (21)$$

where $r_{adj}$ is the apparent zero-flux adjusted spacing and where $\Delta r_x$ and $\Delta r_y$ are the spacing perturbation for the $x$ and $y$ directions, respectively. The subscript numerals also indicate the thermistor number. Equation (21), therefore,

**Table 4.** Estimated Thermal Properties ($\kappa$, $\lambda$, and $C$) From Three PHPPs Comparing Results From Different Calibrated Apparent Spacing ($r_{agar}$, $r_{ins}$, and $r_{adj}$) With Standard Deviation (SD) and Coefficient of Variation ($c_v$) From Water Flux Densities Less Than 2000 cm d$^{-1a}$

| | | $\kappa$ ($10^{-7}$ m$^2$ s$^{-1}$) | | | $\lambda$ (W m$^{-1}$ °C$^{-1}$) | | | $C$ ($10^6$ J m$^{-3}$ °C$^{-1}$) | | |
|---|---|---|---|---|---|---|---|---|---|---|
| | $r$ | Mean | SD | $c_v$ (%) | Mean | SD | $c_v$ (%) | Mean | SD | $c_v$ (%) |
| | $r_{agar}$ | 6.77 | 0.049 | 0.72 | 2.13 | 0.013 | 0.60 | 3.15 | 0.027 | 0.85 |
| PHPP$_{15°}$ | $r_{ins}$ | 6.82 | 0.057 | 0.83 | 2.13 | 0.013 | 0.61 | 3.13 | 0.034 | 1.10 |
| Top | $r_{adj}$ | 6.81 | 0.066 | 0.98 | 2.14 | 0.013 | 0.63 | 3.14 | 0.042 | 1.35 |
| | $r_{agar}$ | 7.59 | 0.066 | 0.86 | 2.24 | 0.016 | 0.71 | 2.95 | 0.016 | 0.53 |
| PHPP$_{30°}$ | $r_{ins}$ | 7.21 | 0.067 | 0.93 | 2.25 | 0.014 | 0.61 | 3.12 | 0.021 | 0.67 |
| Center | $r_{adj}$ | 7.20 | 0.071 | 0.99 | 2.25 | 0.012 | 0.52 | 3.13 | 0.029 | 0.94 |
| | $r_{agar}$ | 7.20 | 0.055 | 0.76 | 2.20 | 0.016 | 0.74 | 3.05 | 0.030 | 0.98 |
| PHPP$_{45°}$ | $r_{ins}$ | 7.07 | 0.043 | 0.61 | 2.21 | 0.018 | 0.81 | 3.13 | 0.016 | 0.51 |
| Bottom | $r_{adj}$ | 7.06 | 0.043 | 0.60 | 2.21 | 0.018 | 0.83 | 3.13 | 0.017 | 0.53 |
| Probe to probe | $r_{agar}$ | 7.19 | 0.335 | 4.66 | 2.19 | 0.045 | 2.08 | 3.05 | 0.082 | 2.68 |
| | $r_{ins}$ | 7.03 | 0.161 | 2.29 | 2.20 | 0.050 | 2.27 | 3.13 | 0.005 | 0.15 |
| | $r_{adj}$ | 7.02 | 0.161 | 2.30 | 2.20 | 0.045 | 2.07 | 3.13 | 0.005 | 0.15 |

[a]Probe-to-probe statistics are also shown.
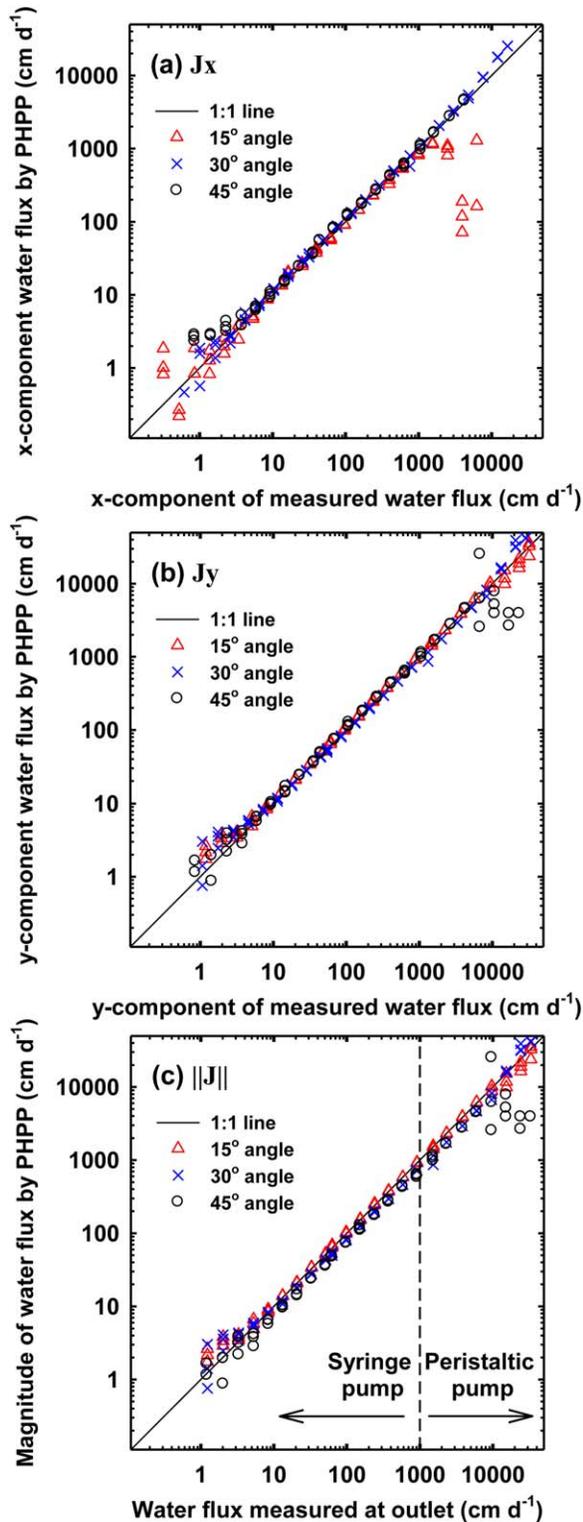
**Figure 7.** Estimated (a) $x$ and (b) $y$ components and (c) magnitude of water flux density estimated by three PHPPs using zero-flux adjusted spacings ($r_{adj}$). The horizontal axes of Figures 7a and 7b indicate the respective component of measured water flux density calculated from the installation angle. Triangle, cross, and circle symbols represent PHPP fluxes installed at 15°, 30°, and 45° angles, respectively. Water flux densities below 1000 cm d$^{-1}$ were controlled by a syringe pump and those above were controlled by a peristaltic pump.

maintains the total distance between S$_1$ and S$_3$ and also between S$_2$ and S$_4$ while adjusting the apparent location of the heater. This fine-tuning procedure described below takes advantage of the in situ spacing calibration values and slightly perturbs $r_{adj}$ (see Table 3) until $V_x$ and $V_y$ approach 0 (i.e., $\sim 10^{-10}$) under no-flow conditions.

[39] The analysis begins with a measured temperature rise data set obtained under no-flow conditions with 0 cm d$^{-1}$ as the known input flux rate. The spacing perturbations, $\Delta r_x$ and $\Delta r_y$, were determined using the following trial and error procedure. (1) Estimate $J_x$ and $J_y$ using the INV-WATFLX code as described previously with $r_{ins}$ spacing estimates (i.e., fitting $\kappa$, $\lambda$, $V_x$, and $V_y$ using $\Delta r_x$ and $\Delta r_y$ values equal to 0 mm). (2) Set the initial $\Delta r_x$ value to 0.1 mm if the calculated $J_x$ overestimates the expected 0 cm d$^{-1}$ flux or set to $-0.1$ mm if the calculated $J_x$ underestimates 0 cm d$^{-1}$. Use the same procedure for setting the initial value of $\Delta r_y$. (3) Calculate $r_{adj}$ values using equation (21). (4) Employ $r_{adj}$ values to estimate $J_x$ and $J_y$ using the INV-WATFLX code (i.e., fitting $\kappa$, $\lambda$, $V_x$, and $V_y$ to temperature rise data measured under the no-flow condition). (5) Compare values of $J_x$ and $J_y$ with the expected 0 cm d$^{-1}$ fluxes. (6) Determine a new $\Delta r_x$ value according to step 2 so that the error estimate of $J_x$ approaches zero (i.e., assuming a liner relationship between $\Delta r_x$ value and the error in $J_x$). The $\Delta r_y$ value is determined similarly. (7) Repeat steps 3–6 until the change in $r_{adj}$ from the previous iteration is less than $10^{-5}$ mm (resulting in $V_x$ and $V_y < 10^{-10}$). Thus, $r_{adj}$ is referred to as the "zero-flux adjusted spacing" calibration. More than three replicate sets of no-flow conditions were used to determine each averaged value of $r_{adj}$. The zero-flux adjusted calibration spacing procedure is also outlined in Table 2.

[40] The final $r_{adj}$ values shown in Table 3 for PHPP$_{15°}$ were obtained using $\Delta r_x = -0.007$ mm and $\Delta r_y = 0.027$ mm. Overall, differences between $r_{ins}$ and $r_{adj}$ are minor for all three PHPP cases. In addition, looking at Table 4 and Figure 4, improvements in optimized values of $\kappa$, $\lambda$, and $C$ for water flux densities below 2000 cm d$^{-1}$ are relatively small when comparing results using $r_{ins}$ and $r_{adj}$. However, Figure 5 shows significant improvements in estimated $J_x$ and $J_y$ below 100 cm d$^{-1}$ using the zero-flux adjusted spacing calibration. Note that $r_{ins}$ is the theoretically optimal spacing based on the objective function in equation (10), which accounts for contact resistance and substrate heterogeneity by fitting measured temperature rise with the analytical solution. On the other hand, $r_{adj}$ is a fine-tuned spacing derived from forcing $V_x$ and $V_y < 10^{-10}$ (i.e., $J_x$ and $J_y = 0$) in order to produce more accurate flux estimation. The effect of "forcing" is that the objective function resulting from the final $r_{adj}$ values may be less optimal than the result using $r_{ins}$. The significance of achieving a flux rate near 1 cm d$^{-1}$ using this novel calibration approach is evidenced by the fact that in only one other study [*Kamai et al.*, 2008] was such a low flux rate achieved, but in that case longer heating times and a larger heater diameter were required to do so. With this in mind, sub-cm d$^{-1}$ flux rates may be possible by combining techniques used by *Kamai et al.* [2008].

### 4.3.2. Two-Component Soil Water Flux Density

[41] Figures 7a and 7b show the estimated $x$ ($J_x$) and $y$ ($J_y$) component water flux densities in addition to the

**Table 5.** RMSE and the Coefficient of Determination ($R^2$) for Estimation of $x$ ($J_x$), $y$ ($J_y$), and Magnitude ($\|\mathbf{J}\|$) of Water Flux Density for Rates Below 7000 cm d$^{-1}$

| | $J_x$ | | $J_y$ | | $\|\mathbf{J}\|$ | |
|---|---|---|---|---|---|---|
| | RMSE (log(cm d$^{-1}$)) | $R^2$ | RMSE (log(cm d$^{-1}$)) | $R^2$ | RMSE (log(cm d$^{-1}$)) | $R^2$ |
| PHPP$_{15°}$ Top | 0.163 | 0.976 | 0.088 | 0.993 | 0.093 | 0.992 |
| PHPP$_{30°}$ Center | 0.157 | 0.980 | 0.107 | 0.989 | 0.092 | 0.992 |
| PHPP$_{45°}$ Bottom | 0.140 | 0.981 | 0.070 | 0.996 | 0.107 | 0.989 |

computed water flux density magnitude exiting the sand column outlet. We tested the three PHPPs with different installation angles across a broad range of water flux density magnitudes from 1.2 to 33,200 cm d$^{-1}$ using all three needle spacing calibrations shown in Table 3. Both $x$ and $y$ components of water flux density estimated from all PHPPs show excellent agreement with the computed water flux densities in the approximate range of 10–7000 cm d$^{-1}$. The RMSE and coefficient of determination, $R^2$, for each PHPP and flow direction are listed in Table 5 where $J_x$ had the largest RMSE of 0.163 (log(cm d$^{-1}$)) and lowest $R^2$ value of 0.976 indicating the excellent 2-D measurement capability of the PHPP using the flux adjusted spacing calibration approach. Furthermore, the PHPP was successful in measuring water flux densities greater than the 2800 cm d$^{-1}$ limit shown in *Mori et al.* [2005]. Water flux density estimates below 10 cm d$^{-1}$ exhibited larger fluctuations on a log-log scale than at higher water flux densities above 10 cm d$^{-1}$ due to the difficulty in detecting upstream and downstream temperature rise differences under low flux conditions. To improve water flux density estimations in the low range, longer heating times or modifications in the structure of the probe (e.g., larger heater diameter) may be needed as suggested in *Kamai et al.* [2008].

[42] Once $x$ and $y$ component water flux densities are estimated with the PHPP, water flux density, $\|\mathbf{J}\|$, can be calculated by equation (14). Figure 7c shows the comparison between estimated $\|\mathbf{J}\|$ and water flow measured at the outlet, which are in excellent agreement (see statistical values in Table 5). Since needle rotation angles were 15°, 30°, and 45° in this study and $y$ component water flux densities were larger than or equal to $x$ component water flux densities, the larger errors observed in $J_x$ for higher flow rates (Figure 7a) had less of an impact on estimation of water flux densities. Although estimated water flux densities fluctuated above the 7000 cm d$^{-1}$ flux range, $c_v$ values calculated from three replicate measurements below 7000 cm d$^{-1}$ exhibited less than 1% variation and excellent reproducibility of the measurements.

### 4.3.3. Water Flux Density Direction

[43] Also of interest is how well the direction of flow can be estimated from the PHPP measurements of water flux density. The 2-D flow field quantified from determination of $J_x$ and $J_y$ using $r_{adj}$ (Figures 7a and 7b) yielded reasonable estimates of the flow angle, $\varphi$, calculated using equation (15). Results from the 24 water flux density steps are plotted as a function of column discharge in Figure 8. Values of $\varphi$ between 10 and 7000 cm d$^{-1}$ were $13.72 \pm 1.49°$ for 15° rotation, $34.14 \pm 0.80°$ for 30° rotation, and

$45.37 \pm 1.51°$ for 45° rotation, showing good agreement with actual water flow direction. Discrepancies between the mean flow angles and the "target" angles are considered minor in light of the difficulty in precisely aligning probe needle angle inserted within the wall of a soil column. Reduced flux determination accuracy below 10 cm d$^{-1}$ and above 7000 cm d$^{-1}$ resulted in substantial scatter in $\varphi$ estimates, with some instances of negative direction.

## 5. Summary and Conclusions

[44] A novel method has been developed to simultaneously estimate soil thermal properties and quantify soil water flux density from fitted temperature rise data using a penta-needle heat pulse probe (PHPP). The method yields estimates of thermal diffusivity, thermal conductivity, and the components of the heat pulse velocity in a 2-D flow field. A new analytical solution of heat conduction and convection in a 2-D domain was developed by extending the analytical solution including 1-D heat convection. These parameters are estimated by making use of a new analytical solution of the heat conduction-convection equation for
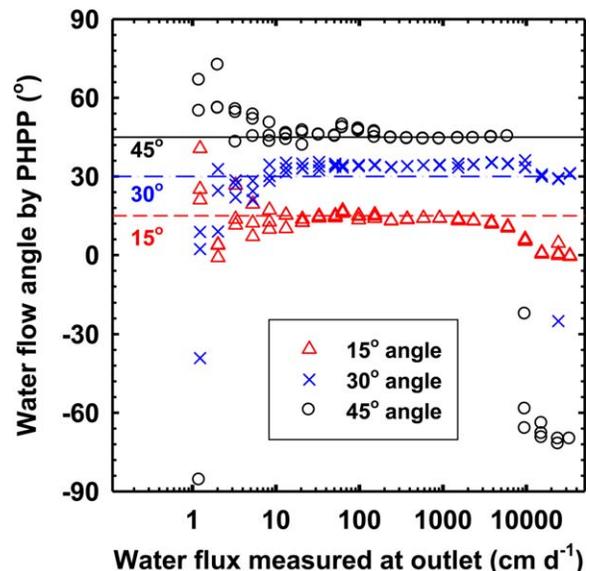


**Figure 8.** Estimated flow angles, $\varphi$, as a function of measured water flux density determined using $r_{adj}$ for the PHPP spacing. Triangle, cross, and circle symbols indicate estimated water flux density angles relative to PHPP installation at 15°, 30°, and 45°, respectively.

pulsed heating of an infinite line source. The Gauss-Newton-Levenberg-Marquardt method is used to solve the inverse problem, which amounts to fitting the analytical solution to a time series of temperature data from the PHPP and optimizing thermal diffusivity ($\kappa$), thermal conductivity ($\lambda$), and the $x$ ($V_x$) and $y$ ($V_y$) components of the heat velocity.

[45] The inverse method was evaluated by conducting a laboratory experiment of water flow in saturated sand with PHPP measurements. A wide range of water flux densities (1.2–33,200 cm d$^{-1}$) were infused, and temperature rise data were obtained with three PHPPs installed at angles of 15°, 30°, and 45° relative to the flow direction. The analytical solution fit well with measured temperature rise from the four thermistors of each PHPP. Thermal properties of $\kappa$, $\lambda$, and heat capacity, $C$ ($=\lambda/\kappa$), were more accurately estimated at water flux densities below 2000 cm d$^{-1}$ if $r$ values were calibrated in situ (i.e., using $r_{ins}$) in the saturated sand column rather than using agar-stabilized spacings, $r_{agar}$. The coefficients of variation under these low flux rates for $\kappa$, $\lambda$, and $C$ were 0.93%, 0.81%, and 1.10%, respectively. Volumetric water content, $\theta$ ($=0.456$), calculated from $C$ agreed well with an estimate based on sand bulk density ($=0.45$).

[46] Seeking improved water flux density estimation accuracy at rates less than 100 cm d$^{-1}$, we found fine tuning of $r_{ins}$ using a zero-flux adjusted spacing, $r_{adj}$, yielded significantly improved estimates down to 1 cm d$^{-1}$. The $r_{adj}$ values were optimized by adjusting estimated $x$ ($J_x$) and $y$ component water flux densities ($J_y$) toward zero, while fitting temperature rise data from a zero-flux condition. The calibration procedure for determining $r_{adj}$ spacings is relatively simple to implement in the optimization code and provides the best estimate of apparent spacing in our study where water fluxes of up to 7000 cm d$^{-1}$ exhibited coefficient of determinations of 0.976 and higher. This led not only to well-estimated $J_x$ and $J_y$ values, but to similarly well-estimated water flux density ($\|\mathbf{J}\|$). Furthermore, water flow angles were also reasonably well estimated between 10 and 7000 cm d$^{-1}$ for all angles, 15°, 30°, and 45°.

[47] We have demonstrated PHPP measurements coupled with a novel inverse method to be very effective in determining soil thermal properties and the components of the soil water flux density and flow direction when zero-flux adjusted spacing, $r_{adj}$, can be accurately determined under no-flow conditions. Further work is needed to assess PHPP performance under unsaturated flow conditions and to extend testing to the field.

## Appendix A

[48] Here we present closed-form expressions for the partial derivatives of equation (7) with respect to the thermal diffusivity ($\kappa$), the thermal conductivity ($\lambda$), the $x$ component of the heat pulse velocity vector ($V_x$), and the $y$ component of the heat pulse velocity vector ($V_y$). These expressions were used to evaluate the entries of the Jacobian matrix given in equation (12). Making use of the function

$$G(x,y,t) = \frac{(x - V_x t)^2 + (y - V_y t)^2}{4\kappa t} \tag{A1}$$

the partial derivatives can be written as

$$\frac{\partial T}{\partial \kappa} = \begin{cases} \dfrac{q'}{4\pi\kappa\lambda} \displaystyle\int_0^t s^{-1} G(x,y,s) e^{-G(x,y,s)} ds; \ 0 < t \le t_0 \\ \dfrac{q'}{4\pi\kappa\lambda} \displaystyle\int_{t-t_0}^t s^{-1} G(x,y,s) e^{-G(x,y,s)} ds; \ t > t_0 \end{cases} \tag{A2}$$

$$\frac{\partial T}{\partial \lambda} = \begin{cases} -\dfrac{q'}{4\pi\lambda^2} \displaystyle\int_0^t s^{-1} e^{-G(x,y,s)} ds; \ 0 < t \le t_0 \\ -\dfrac{q'}{4\pi\lambda^2} \displaystyle\int_{t-t_0}^t s^{-1} e^{-G(x,y,s)} ds; \ t > t_0 \end{cases} \tag{A3}$$

$$\frac{\partial T}{\partial V_x} = \begin{cases} \dfrac{q'}{8\pi\kappa\lambda} \displaystyle\int_0^t s^{-1} (x - V_x s) e^{-G(x,y,s)} ds; \ 0 < t \le t_0 \\ \dfrac{q'}{8\pi\kappa\lambda} \displaystyle\int_{t-t_0}^t s^{-1} (x - V_x s) e^{-G(x,y,s)} ds; \ t > t_0 \end{cases} \tag{A4}$$

and

$$\frac{\partial T}{\partial V_y} = \begin{cases} \dfrac{q'}{8\pi\kappa\lambda} \displaystyle\int_0^t s^{-1} (y - V_y s) e^{-G(x,y,s)} ds; \ 0 < t \le t_0 \\ \dfrac{q'}{8\pi\kappa\lambda} \displaystyle\int_{t-t_0}^t s^{-1} (y - V_y s) e^{-G(x,y,s)} ds; \ t > t_0 \end{cases} \tag{A5}$$

## References

Basinger, J. M., G. J. Kluitenberg, J. M. Ham, J. M. Frank, P. L. Barnes, and M. B. Kirkham (2003), Laboratory evaluation of the dual-probe heat-pulse method for measuring soil water content, *Vadose Zone J.*, *2*(3), 389–399.

Bristow, K. L. (1998), Measurement of thermal properties and water content of unsaturated sandy soil using dual-probe heat-pulse probes, *Agric. For. Meteorol.*, *89*, 75–84.

Bristow, K. L., G. S. Campbell, and K. Calissendorff (1993), Test of a heat-pulse probe for measuring changes in soil water content, *Soil Sci. Soc. Am. J.*, *57*, 930–934.

Bristow, K. L., G. J. Kluitenberg, and R. Horton (1994), Measurement of soil thermal properties with a dual-probe heat-pulse technique, *Soil Sci. Soc. Am. J.*, *58*, 1288–1294.

Campbell, G. S., C. Calissendorff, and J. H. Williams (1991), Probe for measuring soil specific heat using a heat-pulse method, *Soil Sci. Soc. Am. J.*, *55*, 291–293.

Dai, Z., and J. Samper (2004), Inverse problem of multicomponent reactive chemical transport in porous media: Formulation and applications, *Water Resour. Res.*, *40*, W07407, doi:10.1029/2004WR003248.

Endo, A., and M. Hara (2003), Simultaneous measurement of thermal front advection velocity vector and thermal properties of sandy soil under two-dimensional flow field with quintuple-probe heat-pulse technique and its applications, *Trans. Soc. Instrum. Control Eng.*, *2*(12), 88–95.

Endo, A., and M. Hara (2007), Simultaneous measurement of water flux density vectors and thermal properties under drainage conditions in soils, *Paddy Water Environ.*, *5*(3), 171–180.

Gao, J., T. Ren, and Y. Gong (2006), Correcting wall flow effect improves the heat-pulse technique for determining water flux in saturated soils, *Soil Sci. Soc. Am. J.*, *70*(3), 711–717.

Ham, J. M., and E. J. Benson (2004), On the construction and calibration of dual-probe heat capacity sensors, *Soil Sci. Soc. Am. J.*, *68*(4), 1185–1190.

Heitman, J. L., J. M. Basinger, G. J. Kluitenberg, J. M. Ham, J. M. Frank, and P. L. Barnes (2003), Field evaluation of the dual-probe heat-pulse method for measuring soil water content, *Vadose Zone J.*, *2*(4), 552–560.

Hopmans, J. W., J. Šimunek, and K. L. Bristow (2002), Indirect estimation of soil thermal properties and water flux using heat pulse probe measurements: Geometry and dispersion effects, *Water Resour. Res.*, *38*(1), 1006, doi:10.1029/2000WR000071.

Jury W. A., and R. Horton, (2004), *Soil Physics.*, 6th ed., p. 181, John Wiley and Sons, N. Y.

Kamai, T., A. Tuli, G. J. Kluitenberg, and J. W. Hopmans (2008), Soil water flux density measurements near 1 cm d$^{-1}$ using an improved heat pulse probe design, *Water Resour. Res.*, *44*, W00D14, doi:10.1029/2008WR007036.

Kamai, T., A. Tuli, G. J. Kluitenberg, and J. W. Hopmans (2010), Correction to "Soil water flux density measurements near 1 cm d$^{-1}$ using an improved heat pulse probe design," *Water Resour. Res.*, *46*, W07901, doi:10.1029/2010WR009423.

Kluitenberg, G. J., T. E. Ochsner, and R. Horton (2007), Improved analysis of heat pulse signals for soil water flux determination, *Soil Sci. Soc. Am. J.*, *71*(1), 53–55.

Knight, J. H., and G. J. Kluitenberg (2004), Simplified computational approach for dual-probe heat-pulse method, *Soil Sci. Soc. Am. J.*, *68*(2), 447–449.

Knight, J. H., G. J. Kluitenberg, T. Kamai, and J. W. Hopmans (2012), Semianalytical solution for dual-probe heat-pulse applications that accounts for probe radius and heat capacity, *Vadose Zone J.*, *11*(2), doi: 10.2136/vzj2011.0112.

Mori, Y., J. W. Hopmans, A. P. Mortensen, and G. J. Kluitenberg (2003), Multi-functional heat pulse probe for the simultaneous measurement of soil water content, solute concentration, and heat transport parameters, *Vadose Zone J.*, *2*(4), 561–571.

Mori, Y., J. W. Hopmans, A. P. Mortensen, and G. J. Kluitenberg (2005), Estimation of vadose zone water flux from multi-functional heat pulse probe measurements, *Soil Sci. Soc. Am. J.*, *69*(3), 599–606.

Mortensen, A. P., J. W. Hopmans, Y. Mori, and J. Simůnek (2006), Multi-functional heat pulse probe measurements of coupled vadose zone flow and transport, *Adv. Water Resour.*, *29*(2), 250–267.

Nemes, A., M. G. Schaap, F. J. Leij, and J. H. M. Wosten (2001), Description of the unsaturated soil hydraulic database UNSODA version 2.0, *J. Hydrol.*, *251*(3–4), 151–162.

Ochsner, T. E., R. Horton, and T. Ren (2003), Use of the dual-probe heat-pulse technique to monitor soil water content in the vadose zone, *Vadose Zone J.*, *2*(4), 572–579.

Ochsner, T. E., R. Horton, G. J. Kluitenberg, and Q. Wang (2005), Evaluation of the heat pulse ratio method for measuring soil water flux, *Soil Sci. Soc. Am. J.*, *69*(3), 757–765.

Ren, T., G. J. Kluitenberg, and R. Horton (2000), Determining soil water flux and pore water velocity by a heat pulse technique, *Soil Sci. Soc. Am. J.*, *64*(2), 552–560.

Ren, T., T. E. Ochsner, and R. Horton (2003), Development of thermo-time domain reflectometry for vadose zone measurements, *Vadose Zone J.*, *2*(4), 544–551.

Šimůnek, J., and J. W. Hopmans (2002), *Parameter optimization and nonlinear fitting, in Methods of Soil Analysis Part 4 Physical Methods*, edited by J. H. Dane and G. C. Topp, pp. 139–157, Soil Sci. Soc. of Am., Inc., Madison, Wis.

Sisodia, S., and O. J. Helweg (1998), Modeling the heat sense flowmeter, *J. Irrig. Drain. Eng.*, *124*(3), 148–151.

Smits, K. M., T. Sakaki, A. Limsuwat, and T. H. Illangasekare (2010), Thermal conductivity of sands under varying moisture and porosity in drainage-wetting cycles, *Vadose Zone J.*, *9*(1), 172–180, doi:10.2136/vzj2009.0095.

Soil Survey Staff (2003), *National Soil Survey Handbook, Title 430-VI*, U.S. Dep. of Agric., Soil Conserv. Serv., U.S. Gov. Print. Off., Washington, D. C.

Tarara, J. M., and J. M. Ham (1997), Measuring soil water content in the laboratory and field with dual-probe heat-capacity sensors, *Agron. J.*, *89*, 535–542.

Wang, Q., T. E. Ochsner, and R. Horton (2002), Mathematical analysis of heat pulse signals for soil water flux determination, *Water Resour. Res.*, *38*(6), 1091, doi:1010.1029/2001WR001089.

Welch, S. M., G. J. Kluitenberg, and K. L. Bristow (1996), Rapid numerical estimation of soil thermal properties for a broad class of heat-pulse emitter geometries, *Meas. Sci. Technol.*, *7*, 932–938.

Yang, C., and S. B. Jones (2009), INV-WATFLX, a code for simultaneous estimation of soil properties and planer vector water flux from fully or partly functioning needles of a penta-needle heat-pulse probe, *Comput. Geosci.*, *35*(11), 2250–2258.

Yang, C., J. Samper, and J. Molinero (2008), Inverse microbial and geochemical reactive transport models in porous media, *Phys. Chem. Earth*, *33*, 1026–1034.

Young, M. H., G. S. Campbell, and J. Yin (2008), Correcting dual-probe heat-pulse readings for changes in ambient temperature, *Vadose Zone J.*, *7*(1), 22–30.